




Mechanism of hopping conduction in Be–Fe–Al–Te–O semiconducting glasses and glass–ceramics

Natalia A. Wójcik^{1,2,*} , Nagia S. Tagiara³, Doris Möncke^{3,4}, Efstratios I. Kamitsos³, Sharafat Ali², Jacek Ryl¹, and Ryszard J. Barczyński¹

¹Advanced Materials Center, Institute of Nanotechnology and Materials Engineering, Gdańsk University of Technology, 11/12 G. Narutowicza Street, 80-233 Gdańsk, Poland

²Department of Built Environment and Energy Technology, Linnaeus University, 35195 Växjö, Sweden

³Theoretical and Physical Chemistry Institute, National Hellenic Research Foundation, 48 Vassileos Constantinou Avenue, 11635 Athens, Greece

⁴Inamori School of Engineering at the New York State College of Ceramics, Alfred University, 1 Saxon Drive, Alfred, NY 14802, USA

Received: 4 November 2021

Accepted: 14 December 2021

© The Author(s) 2022

ABSTRACT

Electrical properties of beryllium-alumino-tellurite glasses and glass–ceramics doped with iron ions were studied using impedance spectroscopy. The conductivity was measured over a wide frequency range from 10 mHz to 1 MHz and the temperature range from 213 to 473 K. The D.C. conductivity values showed a correlation with the Fe-ion concentration and ratio of iron ions on different valence states in the samples. On the basis of Jonscher universal dielectric response the temperature dependence of conductivity parameters were determined and compared to theoretical models collected by Elliott. In glasses, the conduction process was found to be due to the overlap polaron tunneling while in glass–ceramics the quantum mechanical tunneling between semiconducting crystallites of iron oxides is proposed. The D.C. conductivity was found not to follow Arrhenius relation. The Schnakenberg model was used to analyze the conductivity behavior and the polaron hopping energy and disorder energy were estimated. Additionally, the correlation between alumina dissolution and basicity of the melts was observed.

Introduction

The electrical properties of glasses containing transition metal oxides (TMO) have been of great interest due to their semiconducting nature and potential of

subsequent applications including erasable optical recording media, optical switching devices, laser hosts and second harmonic generation [1–8]. The conduction mechanism in these glasses can be analyzed by several models [9–12], one of which is the

Handling Editor: Kevin Jones.

Address correspondence to E-mail: natalia.wojcik@pg.edu.pl

<https://doi.org/10.1007/s10853-021-06834-w>

Published online: 09 January 2022

well-developed small polaron hopping theory proposed by Mott [9, 10]. The polaron is a quasiparticle of electron with the accompanying local lattice deformation. In this model, the hopping occurs from transition metal ion at lower oxidation state (Fe^{2+}) to a neighboring ion at higher oxidation state (Fe^{3+}). Therefore, the polaron conduction is correlated with the content of iron ions but also with the ratio of iron ions in different valence states and their proximity. However, some models give more satisfactory network parameters and can better explain the variation of conductivity with temperature [12, 13]. As the Mott theory seems to well-describe the conduction behavior of TMO-containing glasses at high temperatures ($> \theta/2$, where θ is Debye temperature) [9], in the low temperature region, the Schnakenberg model can better clarify the variation of activation energy with temperature observed in many glass systems [12, 14]. Schnakenberg considered that an optical multiphonon assisted hopping process determines the D.C. (direct current) conductivity at high temperatures. As the temperature is lowered, multiphonon processes are replaced by a single optical phonon process and at the lowest temperatures the polaron hops with one or more acoustic phonons making up the difference between the sites [12]. This model was found to be in good agreement with the experimental data for many TMO glass systems and gives reasonable values for the phonon frequency, decay parameter, polaron hopping energy and disorder energy [14–16].

TeO_2 glasses doped with high levels of TMO such as V_2O_5 or Fe_2O_3 are known to be good semiconductors [17]. These glasses showed relatively high conductivities of 10^{-4} Scm^{-1} above 400 K. Highly conductive tellurite glasses containing TMOs have potential applicability in electrical devices (e.g., memory switching and gas sensors) [18]. However, to our knowledge, there are so far no reports on electrical properties of BeO containing TeO_2 - Fe_2O_3 glasses and glass-ceramic composites. The Be^{2+} ion is a rather unique cation as it has the highest field strength (charge-to-radius ratio) and electronegativity among all alkaline-earth and alkali ions, and is also characterized by small electronic polarizability, $\alpha(\text{Be}^{2+}) = 0.008 \text{ \AA}^3$ [19]. Therefore, the effect of the addition of BeO on the structure of TeO_2 - Fe_2O_3 glasses and the associated influence on electrical properties is a fascinating topic. In the present study, we report the synthesis and detailed analysis of

electrical properties of Be-Fe-Al-Te-O glasses and glass-ceramics employing different theoretical models.

Materials and methods

Glass preparation

In the present work, five iron-tellurite glasses containing different levels of beryllium oxide were prepared. The glasses have the nominal composition of $x\text{BeO}-10\text{Fe}_2\text{O}_3-(90-x)\text{TeO}_2$ in mol% (designated as 10FexBe), where $x = 0, 10, 15, 20$ and 25 mol%. Appropriate amounts of reagents BeO (99% Alfa Aesar), TeO_2 (99.99% ChemPur GmbH) and Fe_2O_3 (99.9 + % ChemPur GmbH) were thoroughly mixed in a fume hood. Melting was performed in Al_2O_3 crucibles at $900 \text{ }^\circ\text{C}$ for 60 min, under air atmosphere. Melts were poured on a cold brass plate and then were annealed at a temperature of $370 \text{ }^\circ\text{C}$ for 48 h and cooled to room temperature during in 10 h. As shown by ICP OES analysis the uptake of Al_2O_3 is significant and will thus be taken under consideration when discussing the experimental results.

Moreover, the prepared samples will be compared with the glass-ceramic composites doped with two times higher Fe_2O_3 content (20FexBe). Such glass-ceramics were prepared in an analogous way, and the detailed description of their structure and magnetic properties was recently reported [20].

Glass characterization

The amorphous nature of the prepared materials was confirmed by powder X-ray diffraction (XRD). XRD data were collected on a PANalytical PRO MPD instrument with Bragg-Brentano geometry and $\text{CuK}_{\alpha 1}$ radiation over a 2θ range of 10° – 70° at a step size of 0.013° and step time of 52 s. The XRD measurements were conducted at room temperature.

The chemical composition of the samples was investigated using an inductively coupled plasma optical emission spectrometer (ICP OES, Aviro 200 PerkinElmer). Measurements were taken after dissolution of 0.05 g of the respective glass powders in 5 ml of aqueous solution of HF acid (40%). All ICP OES results are listed in Table 1, where the error margins of ICP-OES analysis were $\pm 3\%$ for all elements. The oxygen content was determined from the

Table 1 Glasses ID, target and ICP OES analyzed compositions, optical basicity Λ_{th} , density ρ , iron-ions concentration $N_{Fe-ions}$ and mean Fe–Fe ion spacing R

Sample ID	Target composition (in at%)	ICP OES analyzed glass composition (in at%) $\pm 3\%$	Λ_{th}	ρ (gcm ⁻³)	$N_{Fe-ions}$ ($\times 10^{21}$ cm ⁻³)	R (nm)
xBeO–10Fe ₂ O ₃ –(90-x)TeO ₂						
10Fe0Be	Fe _{6.3} Te _{28.1} O _{65.6}	Fe ₅ Al _{5.1} Te ₂₅ O _{64.9}	0.878	5.06	3.17	0.68
10Fe10Be	Be _{3.2} Fe _{6.5} Te _{25.8} O _{64.5}	Be _{2.5} Fe _{4.9} Al _{3.4} Te _{24.9} O _{64.4}	0.870	5.05	2.96	0.69
10Fe15Be	Be _{4.9} Fe _{6.6} Te _{24.6} O _{63.9}	Be _{2.9} Fe _{6.8} Al _{2.7} Te _{23.6} O ₆₄	0.866	5.05	4.14	0.62
10Fe20Be	Be _{6.7} Fe _{6.7} Te _{23.3} O _{63.3}	Be _{2.8} Fe _{6.8} Al _{2.4} Te ₂₄ O ₆₄	0.869	4.95	4.04	0.63
10Fe25Be	Be _{8.5} Fe _{6.8} Te ₂₂ O _{62.7}	Be ₆ Fe _{5.4} Al _{2.2} Te _{23.1} O _{63.3}	0.846	4.88	3.02	0.69
xBeO–20Fe ₂ O ₃ –(80-x)TeO ₂						
20Fe0Be	Fe _{11.8} Te _{23.5} O _{64.7}	Fe _{9.4} Al _{2.9} Te _{23.2} O _{64.5}	0.883	5.11	6.17	0.55
20Fe10Be	Be ₃ Fe _{12.1} Te _{21.2} O _{63.6}	Be _{2.7} Fe _{9.1} Al _{1.3} Te ₂₃ O _{63.9}	0.872	5.07	5.63	0.56
20Fe15Be	Be _{4.6} Fe _{12.3} Te ₂₀ O _{63.1}	Be _{4.3} Fe _{10.8} Al _{1.7} Te _{20.2} O ₆₃	0.848	5.04	6.67	0.53
20Fe20Be	Be _{6.3} Fe _{12.5} Te _{18.8} O _{62.5}	Be _{5.4} Fe _{12.2} Al _{1.5} Te _{18.6} O _{62.4}	0.836	4.89	7.29	0.52
20Fe25Be	Be _{7.9} Fe _{12.7} Te _{17.5} O _{61.9}	Be _{6.3} Fe _{15.8} Al ₁ Te _{15.8} O _{61.6}	0.821	4.78	9.33	0.47

charge requirements of the analyzed cations. In the case of iron ions, the contents of FeO and Fe₂O₃ were estimated based on XPS measurements. Periodic table mix 1 for ICP measurements (SIGMA-ALDRICH, Products number: 92091) containing Be, Fe, Te and Al ions was used as reference standard.

X-ray photoelectron spectroscopy (XPS) was employed for the surface physicochemical examination of the studied samples. The high-resolution XPS analyses were performed using an Escalab 250Xi device (ThermoFisher Scientific, USA), equipped with a monochromatic AlK α source. The adventitious carbon C 1s peak at 284.6 eV was used for the X-axis calibration of the XPS spectra.

The topography of samples was observed by using an Olympus LEXT OLS4000 Confocal Scanning Laser Microscope (CSLM). Color imaging was performed under white LED light and 3D images were obtained using a 405 nm laser and photomultiplier detector. The maximum used objective lens and laser 3D image magnification was 100x, with optical magnification of 2160x. CSLM measurements were conducted on freshly fractured and alcohol cleaned samples.

The structure of the glasses was studied by Raman and IR spectroscopy. Raman spectra were measured at the backscattering geometry on a Renishaw inVia Raman Microscope equipped with a 2400 lines/mm diffraction grating, a high-sensitivity Peltier-cooled charge coupled device (CCD), a motorized xyz microscope stage and $\times 50$ magnification lens. All measurements were taken in the range from 200 to

2000 cm⁻¹ at room temperature with 2 cm⁻¹ resolution. The 514.5 nm line of an Ar ion laser was used for excitation, employing ca. 0.10 mW/ μ m² at the glass sample to avoid decomposition. Examination of the glasses after the end of each measurement showed no signs of laser-induced modifications when using the Raman microscope. The sample spot size of the Raman microscope is about 0.5 μ m in diameter. Raman spectra were acquired for each glass under VV and VH polarizations, where the first letter indicates the polarization of the exciting laser beam and the second letter the polarization (V: vertical, H: horizontal) of the scattered light. Unpolarized Raman spectra, VV + VH, were also measured. The estimated error in Raman band position was ± 1 cm⁻¹.

The infrared (IR) spectra were measured on a vacuum Fourier-transform spectrometer (Bruker, Vertex 80v) in quasi-specular reflectance mode (11° off-normal). For each spectrum, 400–2000 scans were collected at room temperature with 4 cm⁻¹ resolution and averaged for evaluation. Reflectance spectra were measured separately in the far- and mid-IR ranges and then merged to form a continuous spectrum in the range 30–7000 cm⁻¹. Analysis of the reflectance spectra by Kramers–Kronig transformation yielded the absorption coefficient spectra, $\alpha(\nu)$ [21]. The estimated error in infrared band position was ± 2 cm⁻¹.

Density and electrical properties measurements

Density was evaluated based on Archimedes principle with the use of distilled water as an immersion fluid. The density measurements were conducted three times for each sample. The iron ion concentration ($N_{\text{Fe-ions}}$) given as ions cm^{-3} was calculated based on the measured densities and composition, according to relation:

$$N_{\text{Fe-ions}} = \frac{2 * \rho * n_{\text{Fe}_2\text{O}_3} * N_A}{M_{\text{Fe}_2\text{O}_3}} \quad (1)$$

Here ρ is the glass density (in gcm^{-3}), $M_{\text{Fe}_2\text{O}_3}$ is the molar mass of the Fe_2O_3 (in gmol^{-1}), $n_{\text{Fe}_2\text{O}_3}$ is the Fe_2O_3 mole ratio and N_A is the Avogadro constant. The relationship between N_i and R_i , where R_i is the mean distance between i-ions, is generally described as follows:

$$R_i \approx N_i^{-\frac{1}{3}} \quad (2)$$

This relation is a quite good approximation for calculating the mean distance between i-ions in homogenous glasses where ions are assumed to be distributed uniformly in the glass network. This condition is not fulfilled for samples 20FexBe in which Fe_2O_3 is accumulated in crystallites and, therefore, the R -value is taken here as a rough approximation.

Impedance spectroscopy measurements were conducted in the frequency range from 10 mHz to 1 MHz and the temperature range from 213 to 473 K, with an AC voltage of 1 V_{rms} , using the Novocontrol Concept 40 broadband dielectric spectrometer Alpha-A, equipped with ZG4 dielectric interface. The temperature step was 10 K. For the electrical measurements, gold electrodes were evaporated in vacuum at the polished plane parallel surfaces of circular samples. Measurements were taken under a nitrogen atmosphere using Quatro Cryosystem temperature-controlling system.

Results and discussion

Glass formation and reaction of aluminum crucible with the melt

Table 1 presents the target and measured compositions. The sample names are based on the Fe_2O_3 (10

or 20) and xBeO contents in mol% ($x = 0, 10, 15, 20$ or 20). A significant loss of Be is observed, especially in samples containing lower amount of iron (10FexBe). All melts dissolved also significant amount of aluminum, which originates from the crucible material and is included in the analyzed compositions (see Table 1). The highest amount of Al_2O_3 is observed for samples undoped with BeO in both series (10Fe0Be and 20Fe0Be) and it decreases with an increase in the BeO to the nominal composition as shown in Fig. 1. This phenomena is in contradiction with the observation made for sodium-silicate glasses doped with lithium and beryllium, where the dissolution of Al_2O_3 in the melts was found to be the highest for glasses with the highest BeO amount [22]. Moreover, the content of Al_2O_3 in the present samples is higher than for the ones containing a lower amount of Fe_2O_3 and consequently higher levels of TeO_2 . This can be explained by the high solubility of Al_2O_3 in TeO_2 [23]. Figure 2 presents the density versus beryllium content for all samples. The density decreases with the increase in the Be content. Moreover, similar behavior was found also for the sum of Be and Al concentration as shown in the inset of Fig. 2. This observation can be explained by the light mass and low density of beryllium (1.85 g cm^{-3}) and aluminum (2.7 g cm^{-3}) in comparison with the higher mass and densities of Te (6.24 g cm^{-3}) and Fe (7.87 g cm^{-3}).

Quenching of the beryllium-iron-tellurite melt resulted in black and non-transparent glass samples when considering mm thick pieces. Figure 1 displays exemplar confocal microscope micrographs of the topography of glasses 10Fe0Be (left) and 10Fe20Be (right). The results for other 10FexBe samples are similar and show the homogenous surfaces typical for glassy materials. The amorphous nature of the synthesized 10FexBe samples was confirmed by X-ray diffraction. The absence of any crystalline phases is apparent from Fig. 3. For comparison, the XRD study of 20FexBe samples showed that they are glass-ceramic composites containing Fe_2O_3 crystallites dispersed in the glass matrix [20].

Optical basicity, Λ , is a parameter that often correlates with the level of depolymerization of a conventional glass network where it will be higher as more non-bridging oxygen atoms and ionic bonds occur than for a more polymerized network with covalent bridging bonds between oxygen and network former atoms [24]. In our previous paper [25], we have shown a correlation between glass basicity

Figure 1 Correlation between Al content and the nominal Be content of samples. Two confocal microscope pictures of freshly fractured glasses are also shown: 10Fe0Be (left) and 10Fe20Be (right).

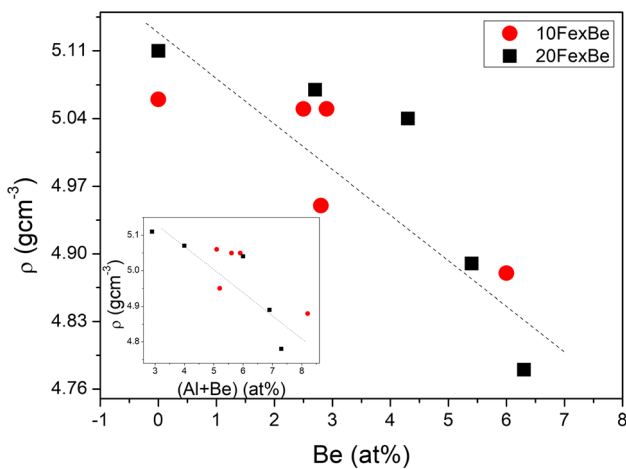
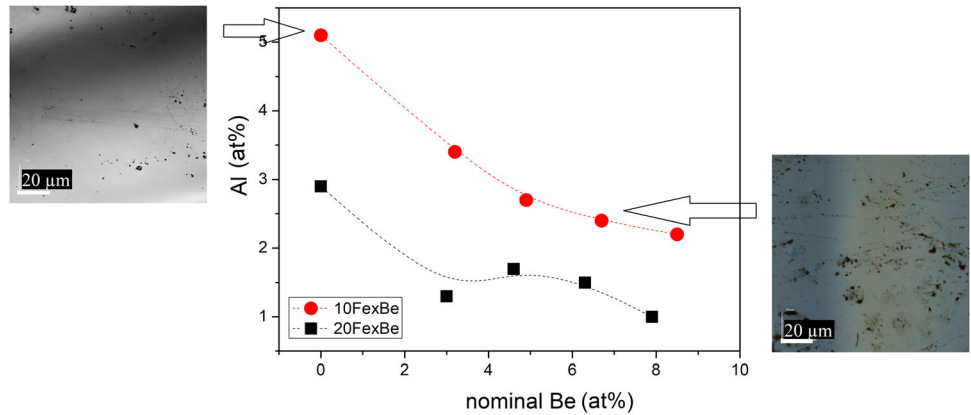


Figure 2 Density as a function of Be content for 10FexBe glasses and 20FexBe glass–ceramics. Inset shows density as a function of the sum of Al and Be contents for 10FexBe glasses and 20FexBe glass–ceramics.

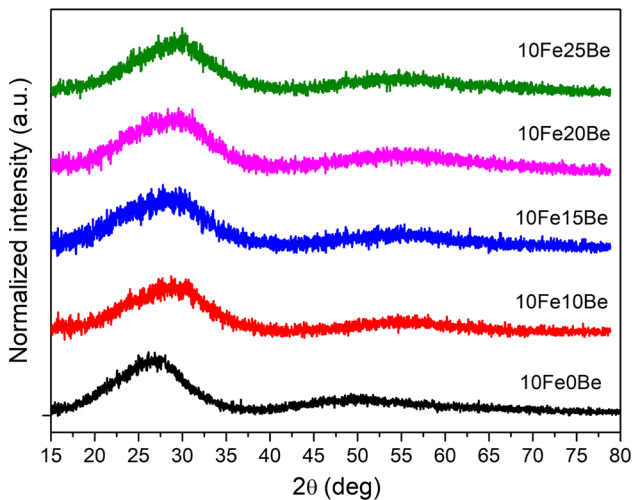


Figure 3 X-ray diffraction spectra of the prepared 10FexBe materials.

calculated on the basis of the glass composition and its role on niobate dissolution from the crucible. Therefore, we examine here the presence of a similar dependence between optical basicity and Al dissolution from the crucible. The theoretical optical basicity for any oxide glass of composition $aA_xO_y - bB_pO_q - \dots$ can be evaluated with the use of the Duffy and Ingram relation [26, 27]:

$$\Lambda_{th} = \frac{X_A}{\gamma_A} + \frac{X_B}{\gamma_B} + \dots$$

$$= \frac{ya}{ya + qb + \dots} \Lambda(A_xO_y) + \frac{qb}{ya + qb + \dots} \Lambda(B_pO_q) + \dots$$

(3)

where $1/\gamma_A = \Lambda(A_xO_y) \dots$ is the optical basicity of oxide A_xO_y , etc. As seen in Eq. (3), the oxide basicities are weighted by their oxygen equivalent fractions X_A , etc., to calculate the glass basicity. Values of Λ for single oxides have been tabulated by various research groups and are constantly expanded to oxides and nitrides of other elements, as well as refined and updated [19, 24, 27, 28]. The values of optical basicity of the studied samples were calculated according to relation (3), using the optical basicity values of the various oxides listed in ref. [29] with $\Lambda(\text{BeO}) = 0.375$, $\Lambda(\text{Fe}_2\text{O}_3) = 0.8$, $\Lambda(\text{FeO}) = 0.93$, $\Lambda(\text{Al}_2\text{O}_3) = 0.61$ and $\Lambda(\text{TeO}_2) = 0.93$, and are reported in Table 1. As can be seen, despite being the network former, the large Te^{4+} cation has a much higher polarizability than the small high field strength modifier cation Be^{2+} , possibly decoupling the polarizability and optical basicity from the degree of polymerization. According to our expectations, Fig. 4a presents an increasing content of dissolved Al with higher optical basicity, especially for the glass series 10FexBe. Therefore, the highest basicity was found for those glasses that

ultimately dissolve the most aluminum indicating that TeO_2 supports Al_2O_3 dissolution. Since higher cation mass (Te, Fe) is correlated to higher polarizability and optical basicity, we see a clear correlation density and optical basicity, as displayed.

Besides obtaining the total Fe content (Table 1), we have carried out XPS measurements for both series to estimate the ratio of iron in its different valence states Fe^{2+} and Fe^{3+} . As an example, the XPS Fe 2p spectrum recorded for sample 20Fe25Be is displayed in Fig. 5a where the proposed deconvolution model consists of four peak doublets. The primary components, with Fe $2p_{3/2}$ located at 710.8 and 712.9 eV, respectively, should be ascribed to Fe^{3+} species like in oxides [30, 31]. Such compounds are always high-spin, leading to complex multiplet split spectra. The smaller component negatively shifted at 709.3 eV lies in the energy range characteristic of Fe^{2+} compounds

[32]. Finally, the broad satellite Fe $2p_{3/2}$ feature typical for iron (III) oxides is distinguishable at approximately 719 eV. Based on the deconvolution results, it is possible to estimate Fe^{2+} and Fe^{3+} relative contents in each studied sample as listed in Table 2 in terms of the ratio $[\text{Fe}^{2+}]/([\text{Fe}^{2+}] + [\text{Fe}^{3+}])$. It can be seen that iron is primarily present in the higher valence state and the content of Fe^{2+} varies between 6.5% (sample 20Fe15Be) and 11.4% (sample 10Fe25Be). This finding is in agreement with earlier studies that showed that a glass matrix of higher optical basicity favors higher oxidation states[33]. However, there is no direct correlation between the composition and the relative content of iron (II) in the studied samples. Moreover, the XPS results confirm that tellurium ions are present only in the Te^{4+} oxidation state in all samples (Fig. 5b). Also, the presence of Al^{3+} ions was confirmed (not shown in graphs), while the Be 1s signal cannot be properly evaluated as it is strongly overlapped by the Te 4d signal.

Short-range-order structure by Raman and infrared spectroscopy

The detailed analysis of the *short-range-order (SRO)* structure of the 20FexBe series was conducted in our previous work [20]. Here, we will focus on the Raman and IR spectra of the 10FexBe series. The polarized Raman spectra are measured in parallel (VV) and cross (HV) polarization to assist the assignment of Raman bands to symmetric (polarized) or asymmetric (depolarized) vibrational modes [34]. The Raman results for the compositions with the lowest (10Fe0Be) and the highest (10Fe25Be) Be content are shown in Fig. 6 (top) and (bottom), respectively. The Raman spectra show three intensive and polarized bands at ~ 447 , ~ 670 and $\sim 765 \text{ cm}^{-1}$ which are attributed to symmetric vibrational modes. The first and most intense band at $\sim 447 \text{ cm}^{-1}$ can be assigned to the symmetric stretching-bending mode of Te–O–Te single bridges, $\nu_s(\text{Te-O-Te})$ [35, 36]. The $\sim 670 \text{ cm}^{-1}$ component can be attributed to the symmetric stretching/breathing mode of Te–O₂–Te double bridges, $\nu_s(\text{Te-O}_2\text{-Te})$, connecting TeO_4 trigonal bipyramids (tbp's) sharing an edge, that is two bridging oxygen atoms [35]. The band at $\sim 765 \text{ cm}^{-1}$ is due to the symmetric stretching of TeO_3^{2-} trigonal pyramids (tp's) with three terminal oxygen atoms, without excluding some contribution from TeO_{3+1} polyhedra [23, 36]. The main difference in the Raman

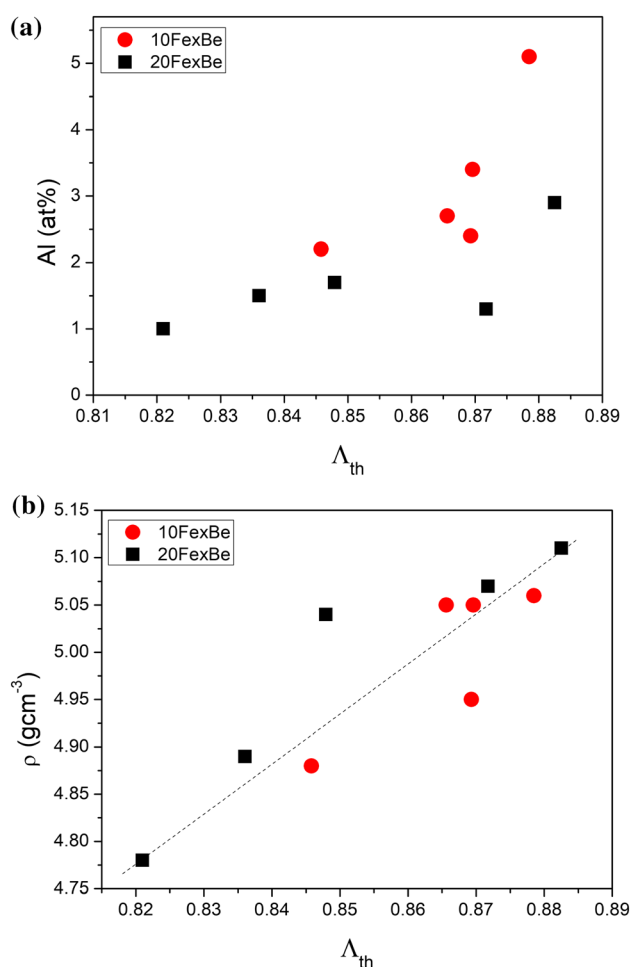


Figure 4 The correlation between optical basicity and Al content (a), and density (b) for all studied samples. Line in (b) is a guide for eyes.

Figure 5 High-resolution XPS spectra recorded in **a** Fe 2p and **b** Te 3d core-level binding energy range for sample 20Fe25Be.

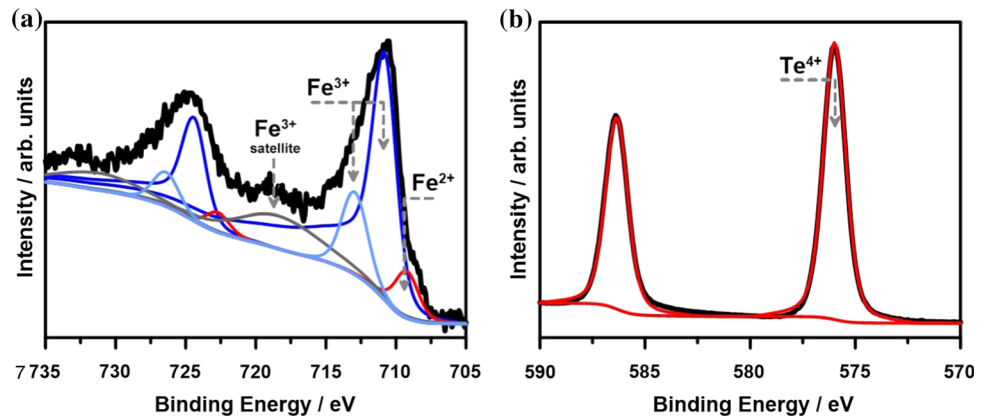


Table 2 D.C. conductivity at 273 K σ_{DC} , and parameters obtained by fitting the conductivity data to the Schnakenberg polaron hopping model (Eq. 6): phonon frequency ν , Debye temperature θ , polaron hopping energy W_H and disorder energy W_D ; mean activation energy at high temperature region W (Eq. 7), total content of Fe-ions [Fe]

(from Table 1), the ratio of Fe-ions on different valence states $C = [Fe^{2+}]/([Fe^{2+}] + [Fe^{3+}])$ (from XPS results), the effective content of Fe-ions which takes part in conduction process $C(1-C)$, and information about structure of samples. The results are given with the mean accuracy of $\pm 95\%$

Sample ID	σ_{DC} at 273 K (S cm ⁻¹)	$\nu \times 10^{13}$ (s ⁻¹)	θ (K)	W_H (eV)	W_D (eV)	W (eV)	[Fe] (at%)	C	C(1-C)	Structure
10Fe0Be	3.47×10^{-11}	3.05	1464	0.64	0.41	0.85	5	0.079	0.073	Amorphous
10Fe10Be	2.07×10^{-11}	2.75	1320	0.67	0.35	0.85	4.9	0.084	0.077	Amorphous
10Fe15Be	6.34×10^{-11}	2.88	1382	0.63	0.38	0.82	6.8	0.079	0.073	Amorphous
10Fe20Be	8.24×10^{-11}	2.88	1382	0.64	0.38	0.83	6.8	0.105	0.094	Amorphous
10Fe25Be	7.80×10^{-11}	2.92	1402	0.78	0.33	0.95	5.4	0.114	0.101	Amorphous
20Fe0Be	4.86×10^{-10}	2.73	1310	0.62	0.33	0.79	9.4	0.088	0.080	Amorphous
20Fe10Be	1.43×10^{-9}	2.04	979	0.59	0.22	0.70	9.1	0.098	0.088	Nanocrystallites
20Fe15Be	1.31×10^{-9}	2.73	1310	0.59	0.33	0.76	10.8	0.065	0.061	Nanocrystallites
20Fe20Be	3.23×10^{-10}	2.70	1305	0.47	0.34	0.64	12.2	0.088	0.080	Nanocrystallites
20Fe25Be	1.84×10^{-9}	2.39	1147	0.55	0.29	0.70	15.8	0.085	0.078	Nanocrystallites

spectra of pure TeO₂ glass [35, 36] and that doped with 5 at% Fe and 5 at% Al (10Fe0Be) is the dominant presence in the latter of the band at ~ 447 cm⁻¹. This intensity enhancement for 10Fe0Be can be correlated with the formation of Al–O–Te and Fe–O–Te bridges, as it was found also for the 20Fe0Be sample [20]. Consequently, the tellurite network of glass 10Fe0Be is more depolymerized than TeO₂ glass through transformation $TeO_4 \rightarrow TeO_{3+1} \rightarrow TeO_3^{2-}$, leading to the formation of Al–O–Te and Fe–O–Te bridges in addition to Te–O–Te bridges.

Comparison in Fig. 6 of the VV polarized Raman spectra of samples before (10Fe0Be) and after doping with BeO (10Fe25Be) shows a slight increase of the relative intensity of the envelopes at ~ 670 cm⁻¹ relative to those at ~ 765 cm⁻¹ and 447 cm⁻¹ after adding BeO. Also, the intensity of the ~ 670 cm⁻¹

band was found to slightly increase relative to that at ~ 765 cm⁻¹ in the order 10Fe15Be < 10Fe20Be < 10Fe25Be, suggesting the increase in content of TeO₄ unit over the TeO₃²⁻ and the TeO₃₊₁ modified tellurite polyhedra [20]. Of interest is also the comparison between samples 10Fe0Be and 10Fe10Be which contain a similar amount of Fe-ions but part of Al³⁺ is substituted by Be²⁺ with a lower valence state. This substitution was found to result in a very slight increase in the polymerization of tellurite network, i.e., increase of the relative content of TeO₄ units.

Unpolarized (VV + VH) Raman spectra for 10FexBe series are displayed in Fig. 7. The results were background corrected and normalized to the stronger band at ~ 447 cm⁻¹ to facilitate comparison. The increase in the intensity of the band at ~ 670 cm⁻¹ relative to that at ~ 765 cm⁻¹ is

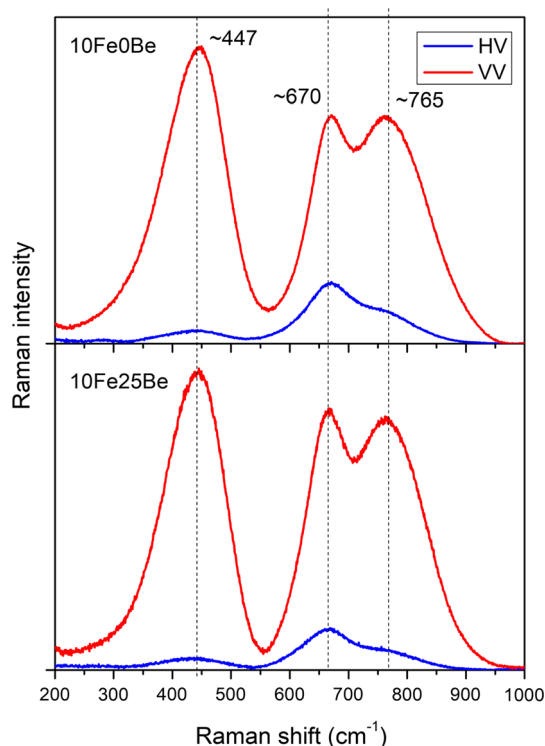


Figure 6 Polarized Raman spectra in parallel (VV, red) and cross (HV, blue) polarization for samples: (a) 10Fe0Be and (b) 10Fe25Be.

noticeable. The observed changes are in accordance with the increase in Be content as well as the total content of all modifiers in glass (10Fe0Be < 10Fe10Be < 10Fe20Be < 10Fe15Be < 10Fe25Be). It suggests the increase in polymerization of the tellurite

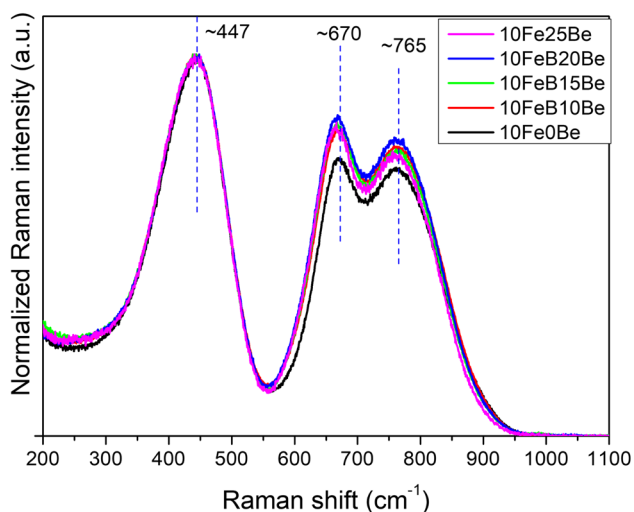


Figure 7 Unpolarized (VV + VH) Raman spectra of all 10FexBe glasses scaled on the 440 cm^{-1} band. Spectra were background corrected and normalized to the band at 440 cm^{-1} .

network for samples doped with BeO in comparison to the undoped one. A similar influence of BeO was observed for samples 20FexBe in which doping with BeO caused also the increase of tellurite network polymerization [20]. It was found that the presence of BeO supported the crystallization process of Fe_2O_3 and, consequently, the residual glass network was poorer in modifier oxides and became more polymerized. In the case of glasses 10FexBe no crystallinity was found, even for the glass with the highest content of BeO. However, a clear correlation between BeO addition and reduction of Al_2O_3 dissolution was noticed. Therefore, most probably the increased polymerization in this case is due to the decrease in the Al content found for beryllium-containing glasses.

To conduct the full analysis of glasses structure, the infrared spectra were also studied and are reported in Fig. 8. IR spectroscopy is complementary to Raman in that the asymmetric vibrational modes of the tellurite network are usually strongly active in the infrared. The main broad and asymmetric IR band is found at $\sim 700 \text{ cm}^{-1}$ and results from the convolution of the asymmetric stretching modes of TeO_3^{2-} , TeO_{3+1} and TeO_4 units [20, 23]. For the pure TeO_2 glass, the strongest infrared absorption band was observed at $\sim 655 \text{ cm}^{-1}$ [35, 36]. For sample 10Fe0Be, the shift to higher frequencies ($\sim 702 \text{ cm}^{-1}$) confirms the presence of the TeO_3^{2-} and TeO_{3+1} units besides TeO_4 units. Moreover, additional broadening at high frequencies may result from weaker contributions of the Al–O stretching in $[\text{AlO}_4/2]^-$ tetrahedra which absorb above 700 cm^{-1} [22]. The slight shift of the main band envelope to lower frequencies is visible for all Be-doped glasses, with sample 10Fe20Be exhibiting the main band at the lowest frequency of $\sim 680 \text{ cm}^{-1}$. This is a confirmation of increasing tellurite network polymerization as observed by Raman spectroscopy. The small envelope at $\sim 463 \text{ cm}^{-1}$ can be correlated with the presence of the modifier Fe ions which in the tellurite network would probably form FeO_6 octahedral units [37]. Finally, the broad and weak envelop at 310 cm^{-1} is mainly due to stretching-bending vibrations of O–Te–O and Te–O–Te bonding in various tellurite configurations [35].

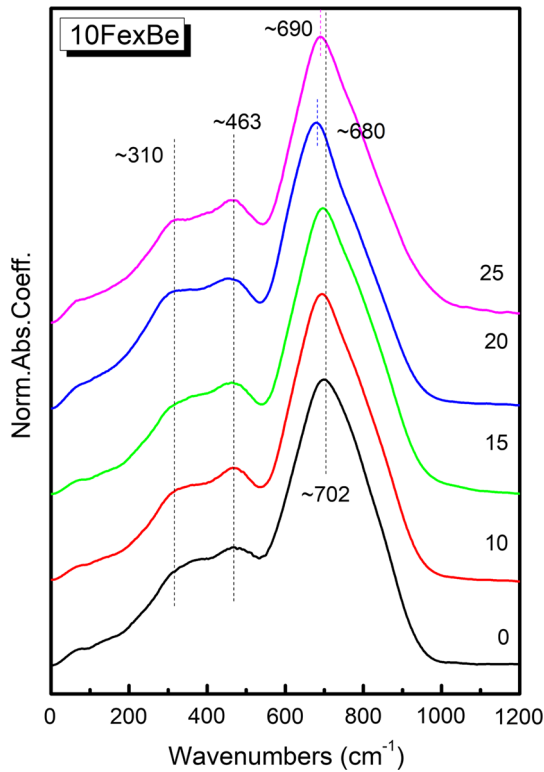


Figure 8 IR spectra of 10FexBe glasses. The spectra are off set for clarity.

Electrical properties

The conductivity behavior was measured for both series of samples 10FexBe and 20FexBe. Figure 9 presents the real part of conductivity as a function of frequency at different temperatures for samples: 10Fe25Be (Fig. 9a), 20Fe20Be (Fig. 9b) and 20Fe25Be (Fig. 9c). The conductivity spectra versus frequency demonstrate a D.C. (direct current) plateau at lower frequencies and an A.C. (alternating current) region of a linear (in log–log scale) increase of conductivity with frequency. Only sample 20Fe20Be was found to show an additional relaxation process in the A.C. part; its shift with temperature suggests that it is thermally activated (Fig. 9b).

The conductivity behavior of almost all tested samples (besides 20Fe20Be) can be analyzed using the Jonscher relation, known also as an universal dynamic response [38]:

$$\text{Re}\sigma(\omega) = \sigma_{\text{DC}}(T) + A(T)\omega^{(sT)} \quad (4)$$

Here $\text{Re}\sigma(\omega)$ is the frequency-dependent real part of conductivity, σ_{DC} is the frequency-independent D.C. conductivity, A is a coefficient and s is an

exponent which depends on temperature and material properties. The part $A\omega^s$ describes the A.C. dispersion. Elliott [39] examined the dependence of the exponent factor s on temperature for various conduction mechanisms in glasses. Here we compare this set of dependencies to values of s estimated from our experimental data by the means of nonlinear data fitting. The obtained values of exponent s are presented versus temperature in Fig. 10. As can be seen the values slightly decrease with the increase in temperature for all samples. In the case of samples 10FexBe and 20Fe0Be s varies between 0.7 and 0.5, while glass–ceramic composites 20Fe10Be, 20Fe15Be and 20Fe25Be exhibit higher values of s between 0.9 and 0.7. For the sample 20Fe20Be the estimation of the s parameter was impossible due to the additional relaxation process at the A.C. part. Comparing the values of exponent s and its temperature behavior to the models discussed by Elliott [39], we suggest that in our homogenous glasses the conduction process may be due to the overlap of polaron tunneling mechanism. In addition, for the glass–ceramics doped with higher content of Fe_2O_3 the quantum mechanical tunneling between semiconducting crystallites of iron oxides can be proposed.

Usually, when the A.C. conductivity of glass comprises relaxation processes the analysis of the impedance spectra can be helpful in determining the conduction mechanisms. Figure 11 (left) displays the Nyquist plot (imaginary versus real part of impedance Z) for sample 20Fe20Be measured at 333 K. Two semicircles are clearly visible, which indicate two relaxation processes. For all other samples, only one distinct and flattened semicircle was observed. The impedance spectra were modeled using the Cole–Cole empirical relation which describes a relaxation by the means of equivalent circuit consisting of a resistance and a CPE (constant phase element and CPE impedance $Z^{-1}_{\text{CPE}} = (j\omega\tau)^{1-\alpha}$) connected in parallel [38, 40]:

$$Z^* = \frac{R}{1 + (j\omega\tau)^{1-\alpha}} \quad (5)$$

where Z^* is the complex impedance, R is the equivalent resistance of a process, τ is the mean dielectric relaxation time, ω is the angular frequency and α is a parameter which describes the width of the relaxation time distribution. For $\alpha = 0$ there is no dispersion (Debye response) and CPE is equivalent to the

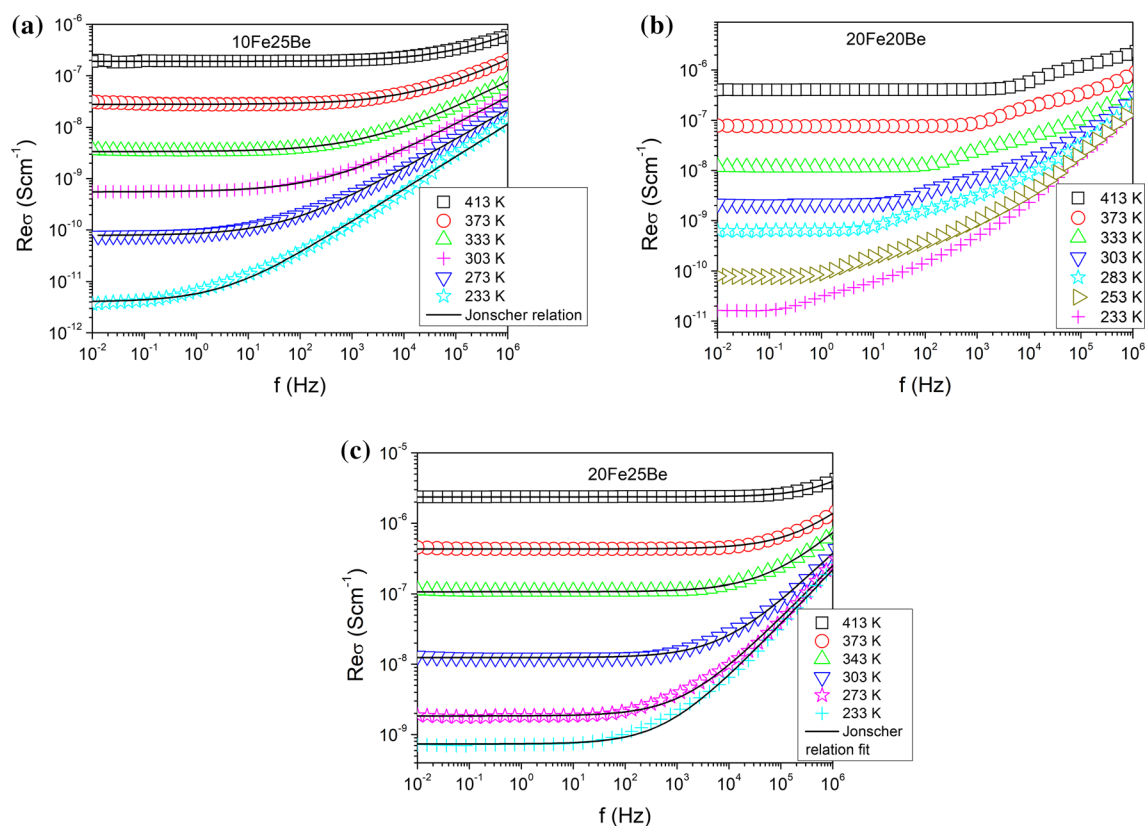


Figure 9 The real part of conductivity versus frequency shown for selected temperatures for (a) 10Fe25Be, (b) 20Fe20Be and (c) 20Fe25Be. The lines present the Jonscher relation fit (Eq. 4).

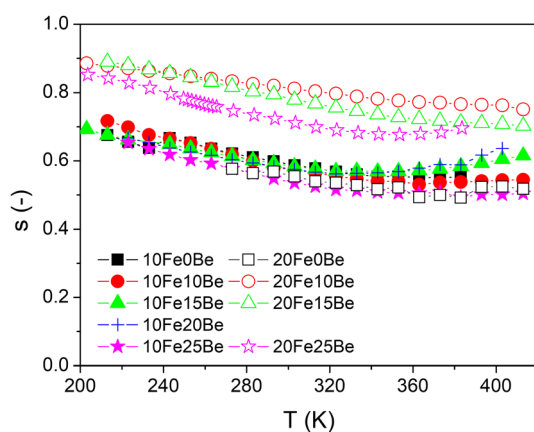


Figure 10 Temperature dependence of s parameter, obtained by fitting the Jonscher relation to conductivity spectra of the studied materials (Eq. 4, Fig. 9).

capacitance, but when $\alpha > 0$ the capacitor cannot be directly defined, reflecting the distributed nature of the response. Our modeling with the use of Cole–Cole relation allows separating components of the conductivity processes taking place through the different composite regions like the crystalline phase

and the amorphous glass matrix. The best fitting results for the sample 20Fe20Be were obtained with a superposition of two Cole–Cole relaxation processes as shown in Fig. 11. The obtained resistivity values were converted to conductivities with the use of sample and electrode sizes and are shown in Fig. 11 (right) as a function of temperature. The conduction process which proceeded at high frequency region exhibits slightly higher conductivity values than the one found at low frequencies. The estimated conductivities do not follow the Arrhenius law suggesting that their activation energy changes with temperature. It was also confirmed based on the analysis of derivative conductivity which was found not to be constant.

Schnakenberg has presented a model for non-adiabatic regime of polaron hopping [12]. According to his model, the activation energy of conductivity changes with temperature and the conductivity versus temperature may be described by [12]:

$$\sigma = \frac{A}{T} \sqrt{\sinh\left(\frac{h\vartheta}{KT}\right)} \exp\left(-\frac{4W_H}{h\nu}\right) \exp\left(-\frac{h\nu}{4KT}\right) \exp\left(-\frac{W_D}{KT}\right) \quad (6)$$

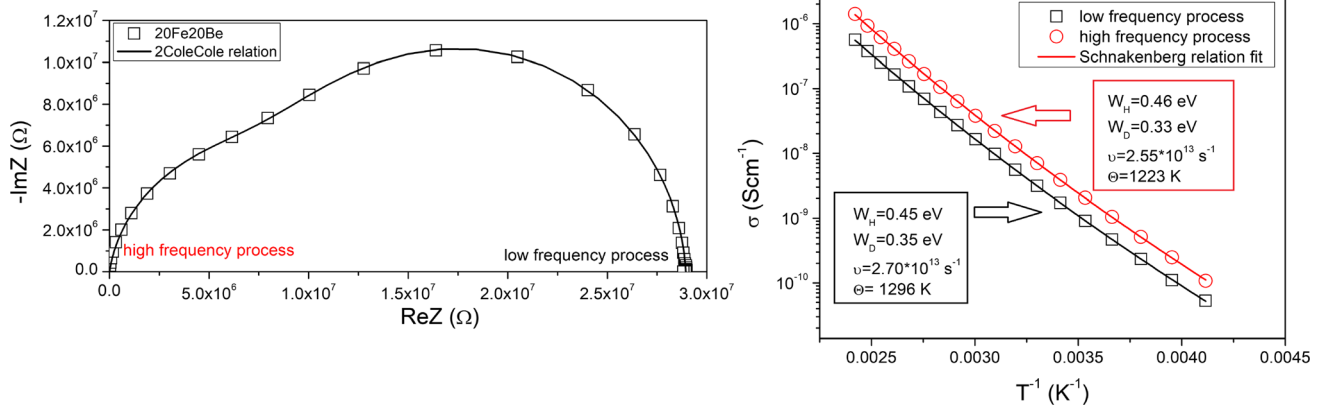


Figure 11 (left) Nyquist plot of sample 20Fe20Be at temperature of 333 K with the fitting results of 2 Cole–Cole relations. (right) Conductivities values of two relaxation processes obtained from fitting the Nyquist plots and the Schnakenberg relation fit results.

where A is a constant, ν is a phonon frequency, W_H is a hopping energy and W_D is a structural disorder energy between hopping sites. Equation (6) is fitted to the data at Fig. 11 (right) and the results are listed in the figure in frames. The fitting results are in good agreement with the experimental data. Interestingly, the obtained values of W_H and W_D of the two relaxation processes (conducted at high and low frequency regions), as well as ν and estimated Debye temperatures θ are close to each other. This suggests that these two conduction processes are due to a similar conduction mechanism: hopping of polarons between iron ions at lower valence state Fe^{2+} to neighboring ion with the higher oxidation level Fe^{3+} . The structure of crystallites is more ordered than the structure of residual glass matrix, therefore slightly lower values of disorder energy and phonon frequency suggest that the high frequency process is due to conduction process within Fe_2O_3 nanocrystallites. The low frequency process is connected with the iron ions dispersed within the residual glass matrix.

The same fitting procedure of Nyquist plots was done for the other glass–ceramics using one and two Cole–Cole relaxations. Significantly better fitting was obtained for the two Cole–Cole relaxations. It suggests that impedance spectra of these materials result from two relaxation processes which strongly overlap. However, as the results of fitting the Schnakenberg relation to conductivity values show similar behavior as for sample 20Fe20Be, we decide to present and compare only the D.C. conductivity behavior to simplify the analysis.

The D.C. conductivity was obtained by fitting the data in Fig. 9 with the Jonscher relation (4) and are plotted in Fig. 12. The D.C. conductivity was found to be higher for samples 20FexBe doped with the highest Fe content. Moreover, a clear correlation between Fe-ion concentration (estimated based on density and Fe content, see Table 1) and the D.C. conductivity values is observed, especially for the glass samples (Fig. 13a). In the case of glass–ceramics, the D.C. conductivity results from the conduction processes through nanocrystallites, the glass matrix and possible grain boundaries. In this case, the D.C. conductivity will not follow strictly the total content of iron ions. Mott [9] noticed that polaron jumps between nearest neighboring ions are possible when they are of different valence states. If C is the ratio

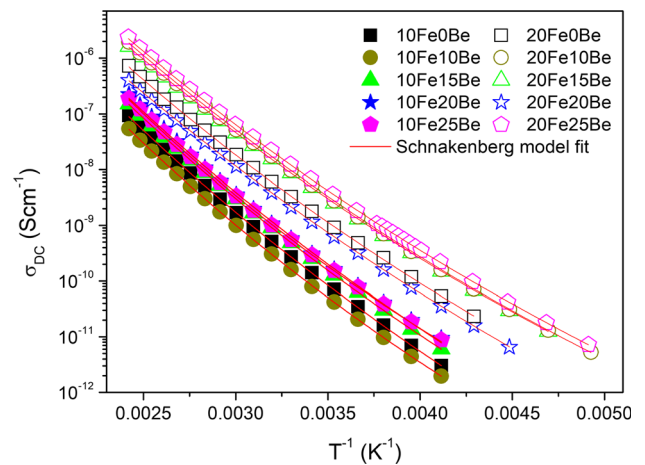


Figure 12 D.C. conductivity estimated from Figs. 9 (Eq. 4) as a function of temperature. Lines shows the Schnakenberg model fit (Eq. 6). The mean adjusted R^2 value of fitting was found to be 0.999 for all samples.

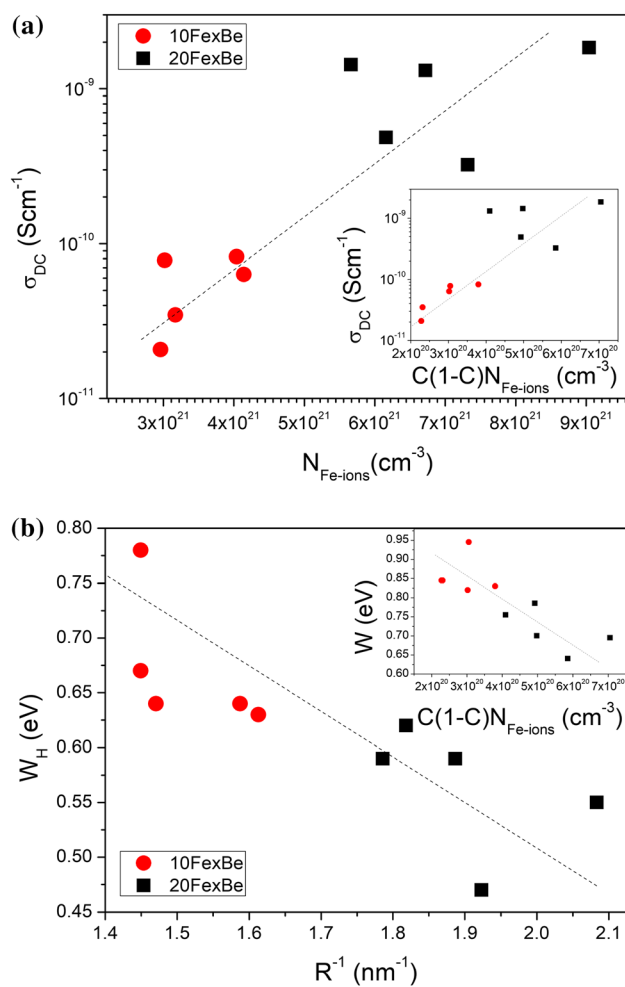


Figure 13 (a) D.C. conductivity at 273 K as a function of iron ion concentration for all studied samples. Inset in (a) shows the correlation of D.C. conductivity and effective concentration of iron ions taking place in the conduction process for all samples. (b) Polaron hopping energy versus mean iron ions spacing. Inset in (b) displays the high temperature activation energy estimated on the basis of Eq. 7 as a function of effective concentration of iron ion taking place in conduction process.

between the concentration of transition metal ions in the low valence state to the total concentration of transition metal ions, $C = [\text{Fe}^{2+}]/([\text{Fe}^{2+}] + [\text{Fe}^{3+}])$ then concentration of hopping sites is proportional to $C(1-C)$. A correlation between D.C. conductivity and $C(1-C)$ multiplied by the Fe-ion concentration is visible (inset of Fig. 13a). It confirms that in our samples, the conductivity of homogenous glasses is mostly influenced by the effective concentration of carriers participating in charge transport. The D.C. conductivity shows good agreement with Schnakenberg relation (red lines in Fig. 12). Analysis of

Schnakenberg relation (6) fitting results is listed in Table 2 for all samples. It is apparent that W_H and W_D values found for glass–ceramics are lower than for glasses, and this was associated to the higher amount of carriers. The highest value of disorder was achieved for glass 10Fe0Be which also showed the highest depolymerization of the tellurite network of all glasses. The lowest value of hopping energy was detected for the sample 20Fe20Be in which the effect of nanocrystallites was also clearly visible in the impedance spectra.

It was shown by Mott that the hopping energy is $W_H \sim r_p^{-1} - R^{-1}$, where R is a mean distance between iron ions (listed in Table 1) and r_p is the polaron radius [9]. In the case of overlap polaron hopping $r_p \ll R$, and therefore W_H should show a dependence on R as found for our samples in Fig. 13b. The hopping energy decreases as the mean distance between iron ions decreases. At the high temperature region the activation energy W , arising from electron-lattice interactions and static disorder, is given by:

$$W = W_H + \frac{W_D}{2}, \quad T > \frac{\theta_D}{2} \quad (7)$$

where θ_D is Debye temperature ($\theta_D = h\nu/K$, h is the Planck's constant). The values of estimated W values are listed in Table 2 and plotted in the inset of Fig. 13b as a function of the effective concentration of carriers taking place in the transport. It can be seen that the estimated activation energy decreases with the increase in carrier concentration for both series of samples. The values of phonon frequencies obtained from fitting the Schnakenberg relation (Table 2) appear to be larger than typical ones (10^{13} s^{-1} rather than 10^{12} s^{-1}); however, similar high results were found for vanadate-tellurite glasses [15]. The phonon frequency was used to estimate the Debye temperature for all samples (Table 2). Like the phonon frequencies, the Debye temperatures were found to be rather high, i.e., between 979 and 1464 K. However, it is hard to define the meaning of a Debye temperature in disordered materials, in analogy to the temperature of a crystal corresponding to highest frequency normal mode of vibration.

Conclusions

Beryllium tellurite glasses with high iron content were prepared and studied for their structure and properties, with a special emphasis on their electrical properties. The glasses contained significant amounts of alumina from crucible dissolution. The series containing 10 mol% Fe₂O₃ was amorphous, while the earlier studies series with 20 mol% Fe₂O₃ was partially crystallized. Divalent Fe²⁺ was identified by XPS as a minority species with a ratio to the total Fe content less than 0.11. Infrared and Raman spectroscopy showed only minor structural changes as BeO replaces TeO₂ in the xBeO–10Fe₂O₃–(90–x)TeO₂ series. Contrary to conventional glasses, where the network modifier such as Si, B or P has a lower polarizability than the network modifier, is the high field strength cation Be²⁺ less polarizable than the large Te⁴⁺ network former cation. Alumina dissolution seems to be linked to the basicity of the melts rather than the number of non-bridging oxygen atoms, and through the dissolution of the crucible material Al₂O₃ is taken up by the melt, which in turn heightens the number of non-bridging oxygen in the BeO poor, high basicity glasses.

The comparison of Jonscher universal dielectric response and theoretical models collected by Elliott revealed that in glasses the conduction process is due to the overlap polaron tunneling. In glass–ceramics the quantum mechanical tunneling between semi-conducting crystallites of iron oxides is proposed as a secondary mechanism. The D.C. conductivity behavior was analyzed based on the Schnakenberg model and the energy of polaron hopping and disorder were estimated. Fitting model parameters show that phonon frequency is rather high and polaron energy term due to disorder is larger in glasses than for glass–ceramics.

Acknowledgements

We want to thank Hiroyo Segawa for ICP-OES measurements and Karolina Górnicka for XRD measurements. NAW and SA acknowledge support by the STINT (Grant No. MG 2018-7558). NST and EIK acknowledge support by the project “National Infrastructure in Nanotechnology, Advanced Materials and Micro-/Nanoelectronics” (MIS 5002772), funded by the Operational Programme

“Competitiveness, Entrepreneurship and Innovation” (NSRF 2014-2020) and co-financed by Greece and the European Union (European Regional Development Fund).

Author contributions

NAW contributed to investigation, validation, methodology, writing—original draft, visualization; NST, JR helped in methodology, writing—review and editing, visualization; DM, EIK, SA, RJB contributed to supervision, writing—review and editing.

Data availability

The data that support the findings of this study are available from the corresponding author upon reasonable request.

Declarations

Conflict of interest The authors wish to confirm that there are no known conflicts of interest associated with this publication and there has been no significant financial support for this work that could have influenced its outcome. J Mater Sci manuscript has been read and approved by all named authors.

Open Access This article is licensed under a Creative Commons Attribution 4.0 International License, which permits use, sharing, adaptation, distribution and reproduction in any medium or format, as long as you give appropriate credit to the original author(s) and the source, provide a link to the Creative Commons licence, and indicate if changes were made. The images or other third party material in this article are included in the article’s Creative Commons licence, unless indicated otherwise in a credit line to the material. If material is not included in the article’s Creative Commons licence and your intended use is not permitted by statutory regulation or exceeds the permitted use, you will need to obtain permission directly from the copyright holder. To view a copy of this licence, visit <http://creativecommons.org/licenses/by/4.0/>.

References

- [1] Barczyński RJ, Król P, Murawski L (2010) Ac and dc conductivities in V_2O_5 - P_2O_5 glasses containing alkaline ions. *J Non-Cryst Solids* 356(37–40):1965–1967. <https://doi.org/10.1016/j.jnoncrysol.2010.07.001>
- [2] Barczyński RJ, Szreder NA, Karczewski J, Gazda M (2014) Electronic conductivity in the SiO_2 - PbO - Fe_2O_3 glass containing magnetic nanostructures. *Solid State Ionics* 262:801–805. <https://doi.org/10.1016/j.ssi.2013.10.008>
- [3] Szreder NA, Barczyński RJ, Karczewski J, Gazda M (2014) Electrical properties and structure of lead-borate glass containing iron ions. *Solid State Ionics* 262:837–840. <https://doi.org/10.1016/j.ssi.2014.01.042>
- [4] Lenarciak A, Wójcik NA, Kupracz P, Strychalska-Nowak J, Sobczak Z, Przeźniak-Welenc M, Karczewski J, Barczyński RJ (2019) Thermal, electrical, and magnetic properties of Fe_2O_3 - PbO - SiO_2 glass prepared by traditional melt-quenching and twin roller fast-cooling methods. *J Phys Chem Solids* 135:109010. <https://doi.org/10.1016/j.jpcs.2019.05.007>
- [5] Vora AM (2007) Superconducting state parameters of $CuCrZr_{100}$ -C metallic glasses. *Front Phys* 2(4):430–435. <https://doi.org/10.1007/s11467-007-0053-0>
- [6] Wen B, Cao M, Lu M, Cao W, Shi H, Liu J, Wang X, Jin H, Fang X, Wang W, Yuan J (2014) Reduced graphene oxides: light-weight and high-efficiency electromagnetic interference shielding at elevated temperatures. *Adv Mater (Deerfield Beach, Fla)* 26(21):3484–3489. <https://doi.org/10.1002/adma.201400108>
- [7] Wen B, Cao M-S, Hou Z-L, Song W-L, Zhang L, Lu M-M, Jin H-B, Fang X-Y, Wang W-Z, Yuan J (2013) Temperature dependent microwave attenuation behavior for carbon-nanotube/silica composites. *Carbon* 65:124–139. <https://doi.org/10.1016/j.carbon.2013.07.110>
- [8] Gong P, Yang Y-Y, Ma W-D, Fang X-Y, Jing X-L, Jia Y-H, Cao M-S (2021) Transport and recombination properties of group-III doped SiCNTs. *Physica E Low-Dimens Syst Nanostructures* 128:114578. <https://doi.org/10.1016/j.physe.2020.114578>
- [9] Mott NF (1968) Conduction in glasses containing transition metal ions. *J Non-Cryst Solids* 1:1–17. [https://doi.org/10.1016/0022-3093\(68\)90002-1](https://doi.org/10.1016/0022-3093(68)90002-1)
- [10] Austin IG, Mott NF (1969) Polarons in crystalline and non-crystalline material. *Adv Phys* 18:41–102. <https://doi.org/10.1080/00018736900101267>
- [11] Holstein T (1959) Studies of polaron motion: Part II. *Ann Phys NY* 8:343–389. [https://doi.org/10.1016/0003-4916\(59\)90003-X](https://doi.org/10.1016/0003-4916(59)90003-X)
- [12] Schnakenberg J (1968) Polaronic impurity hopping conduction. *Phys Status Solidi (b)* 28(2):623–633. <https://doi.org/10.1002/pssb.19680280220>
- [13] Gorham-Bergeron E, Emin D (1977) Phonon-assisted hopping due to interaction with both acoustical and optical phonons. *Phys Rev B* 15(8):3667–3680. <https://doi.org/10.1103/PhysRevB.15.3667>
- [14] Szreder NA, Kosiorek P, Karczewski J, Gazda M, Barczyński RJ (2014) Microstructure and dielectric properties of barium-vanadate glasses. *Procedia Eng* 98:62–70. <https://doi.org/10.1016/j.proeng.2014.12.489>
- [15] Mansour E, Korna A, el Damrawi G (2005) Single and multiphonon assisted hopping conduction in CoO - TeO_2 - V_2O_5 glasses. *Phys Chem Glasses Eur J Glass Sci Technol B* 46:21–26
- [16] Mansour E, El-Egili K, El-Damrawi G (2007) Mechanism of hopping conduction in new CeO_2 - B_2O_3 semiconducting glasses. *Physica B* 389(2):355–361. <https://doi.org/10.1016/j.physb.2006.07.017>
- [17] El-Desoky MM (2005) Characterization and transport properties of V_2O_5 - Fe_2O_3 - TeO_2 glasses. *J Non-Cryst Solids* 351(37):3139–3146. <https://doi.org/10.1016/j.jnoncrysol.2005.08.004>
- [18] Murawski L (1982) Electrical conductivity in iron-containing oxide glasses. *J Mater Sci* 17(8):2155–2163. <https://doi.org/10.1007/BF00543723>
- [19] Dimitrov V, Komatsu T (2010) An interpretation of optical properties of oxides and oxide glasses in terms of the electronic ion polarizability and average single bond strength. *J Univ Chem Technol Metall* 45(3):219–250
- [20] Wójcik NA, Tagiara NS, Ali S, Górnicka K, Segawa H, Klimczuk T, Jonson B, Möncke D, Kamitsos EI (2021) Structure and magnetic properties of BeO - Fe_2O_3 - Al_2O_3 - TeO_2 glass-ceramic composites. *J Eur Ceram Soc*. <https://doi.org/10.1016/j.jeurceramsoc.2021.04.005>
- [21] Kamitsos EI (2015) Infrared spectroscopy of glasses. In: Affatigato M (ed) *Modern glass characterization*. John Wiley & Sons Inc, New Jersey, pp 32–73. <https://doi.org/10.1002/9781119051862.ch2>
- [22] Wójcik NA, Ali S, Möncke D, Tagiara NS, Kamitsos EI, Segawa H, Eriksson M, Jonson B (2019) The influence of Be addition on the structure and thermal properties of alkali-silicate glasses. *J Non-Cryst Solids* 521:119532. <https://doi.org/10.1016/j.jnoncrysol.2019.119532>
- [23] Tagiara NS, Moayedi E, Kyritsis A, Wondraczek L, Kamitsos EI (2019) Short-range structure, thermal and elastic properties of binary and ternary tellurite glasses. *J Phys Chem B* 123(37):7905–7918. <https://doi.org/10.1021/acs.jpcc.9b04617>

- [24] Möncke D, Ali S, Jonson B, Kamitsos EI (2020) Anion polarizabilities in oxynitride glasses. Establishing a common optical basicity scale. *Phys Chem* 22(17):9543–9560. <https://doi.org/10.1039/C9CP06930E>
- [25] Wójcik NA, Ali S, Kamitsos EI, Möncke D (2022) Niobate in silicate and phosphate glasses: Effect of glass basicity on crucible dissolution. *Int J Appl Glass Sci* 13(1):121–134. <https://doi.org/10.1111/ijag.16505>
- [26] Duffy JA, Ingram MD (1971) Establishment of an optical scale for Lewis basicity in inorganic oxyacids, molten salts, and glasses. *J Am Chem Soc* 93(24):6448–6454. <https://doi.org/10.1021/ja00753a019>
- [27] Duffy JA (1993) A review of optical basicity and its applications to oxidic systems. *Geochim Cosmochim Acta* 57(16):3961–3970. [https://doi.org/10.1016/0016-7037\(93\)90346-X](https://doi.org/10.1016/0016-7037(93)90346-X)
- [28] Duffy JA (2011) Oxidic glasses as hosts for migrating metal ions. *J Solid State Electrochem* 15(1):87–93. <https://doi.org/10.1007/s10008-009-0980-5>
- [29] Rodriguez C, McCloy J, Schweiger M, Crum J, Winschell A (2011) Optical basicity and nepheline crystallization in high alumina glasses. <https://doi.org/10.2172/1019213>
- [30] Wang J-C, Ren J, Yao H-C, Zhang L, Wang J-S, Zang S-Q, Han L-F, Li Z-J (2016) Synergistic photocatalysis of Cr(VI) reduction and 4-Chlorophenol degradation over hydroxylated α -Fe₂O₃ under visible light irradiation. *J Hazard Mater* 311:11–19. <https://doi.org/10.1016/j.jhazmat.2016.02.055>
- [31] Makarova I, Ryl J, Sun Z, Kurilo I, Górnicka K, Laatikainen M, Repo E (2020) One-step recovery of REE oxalates in electro-leaching of spent NdFeB magnets. *Sep Purif Technol* 251:117362. <https://doi.org/10.1016/j.seppur.2020.117362>
- [32] Mandal SK, Rakshit T, Ray SK, Mishra SK, Krishna PSR, Chandra A (2013) Nanostructures of Sr²⁺ doped BiFeO₃ multifunctional ceramics with tunable photoluminescence and magnetic properties. *J Phys Condens Matter* 25(5):055303. <https://doi.org/10.1088/0953-8984/25/5/055303>
- [33] Duffy JA (1996) Redox equilibria in glass. *J Non-Cryst Solids* 196:45–50. [https://doi.org/10.1016/0022-3093\(95\)00560-9](https://doi.org/10.1016/0022-3093(95)00560-9)
- [34] Efthimiopoulos I, Palles D, Richter S, Hoppe U, Möncke D, Wondraczek L, Nolte S, Kamitsos EI (2018) Femtosecond laser-induced transformations in ultra-low expansion glass: microstructure and local density variations by vibrational spectroscopy. *J Appl Phys* 123(23):233105. <https://doi.org/10.1063/1.5030687>
- [35] Papadopoulos AG, Tagiara NS, Simandiras ED, Kamitsos EI (2020) On the absence of doubly bonded Te=O groups in TeO₂ glass. *J Phys Chem B* 124(27):5746–5753. <https://doi.org/10.1021/acs.jpcc.0c02499>
- [36] Tagiara NS, Palles D, Simandiras ED, Psycharis V, Kyritsis A, Kamitsos EI (2017) Synthesis, thermal and structural properties of pure TeO₂ glass and zinc-tellurite glasses. *J Non-Cryst Solids* 457(Supplement C):116–125. <https://doi.org/10.1016/j.jnoncrysol.2016.11.033>
- [37] Rada S, Dehelean A, Culea E (2010) FTIR, Raman, and UV–Vis spectroscopic and DFT investigations of the structure of iron–lead–tellurate glasses. *J Mol Model* 17:2103–2111. <https://doi.org/10.1007/s00894-010-0911-5>
- [38] Jonscher AK (1977) Universal dielectric response. *Nature* 267(5613):673–679. <https://doi.org/10.1038/267673a0>
- [39] Elliott SR, Owens AP (1989) The diffusion-controlled relaxation model for ionic transport in glasses. *Philos Mag B* 60(6):777–792. <https://doi.org/10.1080/13642818908209742>
- [40] Macdonald J (ed) (1987) Impedance spectroscopy: emphasizing solid materials and systems. John Wiley & Sons, New York, pp 1–346

Publisher's Note Springer Nature remains neutral with regard to jurisdictional claims in published maps and institutional affiliations.